Title

Intensification of a rain system imparted by Mediterranean mesoscale eddies.

Journal

Scientific Reports, 14(1)

Authors

Strobach, Ehud

Mishra, Alok

Jangir, Babita

et al.

Publication Date

2024-11-05

DOI

10.1038/s41598-024-76767-2

Peer reviewed

scientific reports

Check for updates

OPEN

Intensification of a rain system imparted by Mediterranean mesoscale eddies

Ehud Strobach[1]✉, Alok Kumar Mishra[1], Babita Jangir[1], Baruch Ziv[2], Rui Sun[3], Lia Siegelman[3], Agostino Niyonkuru Meroni[4] & Patrice Klein[5,6]

Ocean mesoscale eddies, with $20-300$ km size, present in energetic regions of the global ocean, are known to impact local and remote atmospheric weather. The impact of eddies in the Mediterranean Sea on the local weather, however, remains largely unknown. Here, we study this impact during an extreme weather event observed over Israel on January $8-10$, 2020, resulting in heavy rains and floods. To do so, we designed a set of coupled and forced numerical simulations with a horizontal resolution of 5 km in both ocean and atmosphere. The coupled simulation successfully reproduces the main characteristics of the torrential rains observed during the event, whereas the forced simulations exhibit poorer performance. Our results emphasize the importance of mesoscale air-sea coupling in supplying moisture to the atmosphere, via mechanisms involving both sea surface temperature and surface currents associated with sea eddies. Extreme weather events are intensified by the Mediterranean Sea eddies, especially through atmospheric meso-cyclones.

The ocean interacts with the atmosphere through the exchange of heat, water, and momentum. While this interaction is considered small on long-term time scales and large-scale space scales[1,2], several studies from recent years have shown its importance in reproducing extreme precipitation events such as atmospheric rivers, monsoons, and storms[3–11].

Ocean mesoscale eddies of 20 to 300 km (hereafter mesoscale eddies) contain 80 % of the kinetic energy in oceans and seas[12,13]. They are now known to impact the atmosphere, with an emphasis on precipitations, through their associated sea surface temperature (SST) anomalies[14–16]. This is particularly true in winter, when SST anomalies are closely related to mesoscale eddies with a phase shift similar to what is expected from baroclinic instability[2,17–19]. Meso and sub-mesoscale SST fronts are also known to modulate heavy rains[20–22]. Because of the asymmetric response of warm and cold eddies to air-sea interactions, mesoscale eddies alone explain 15% to 30% of the total surface heat fluxes (including latent heat fluxes (LHF), a source of moisture) in winter, which intensifies extratropical storms[23,24]. Subsequently, these atmospheric storms transport moisture downwind, leading to heavy rains when they make landfall on mountainous coasts. These mechanisms in mesoscale eddies were shown by Liu et al. (2021)[14] to explain 20% to 30 % of the heavy precipitations over the west coast of the US.

Like Western Boundary Currents (WBCs), the Mediterranean Sea (MS) is characterized by high sea eddy activity[25–27]. However, MS eddies are typically smaller in size (< 100 km diameter) and have a shorter time scale (less than two weeks) than in WBCs[27–29]. In winter, the Eastern Mediterranean region is characterized by two main storm tracks: a northern track to the south of the Black Sea and a southern track centered in the north part of the Eastern MS[30–32]. The cyclones of the southern track typically land on the Eastern coast of the MS and are the main precipitation source for Israel. Atmospheric meso-cyclones (∼500 km size) are also present over the MS. These mesoscale storms, which are smaller than mid-latitude synoptic atmospheric storms (∼1500 km size), have a high impact on precipitations, in particular over mountainous coasts[33]. Also, when interacting with complex topography, mesoscale convective systems have been shown to be related to flash floods[34]. Mesoscale SST structures have been found to affect the atmospheric dynamics (in terms of wind, clouds, and rainfall) over the MS on daily time scales[9,10,35,36] and longer[37]. The interaction between mesoscale eddies and cyclones in the Mediterranean region has not been studied yet.

The current study focuses on one specific atmospheric event related to the above-mentioned southern storm track in the Eastern MS. This event was chosen due to its exceptional daily rainfall, massive flood damage, and loss of lives. Using a set of numerical simulations, we investigate the effects of the air-sea coupling and

[1]Agricultural Research Organization, Rishon LeTsiyon, Israel. [2]The Open University of Israel, Ra'anana, Israel. [3]Scripps Institution of Oceanography, UC San Diego, San Diego, USA. [4]University of Milano-Bicocca, Milan, Italy. [5]Jet Propulsion Laboratory, California Institute of Technology, Pasadena, CA 91109, USA. [6]LMD/IPSL, CNRS, Ecole Normale Supérieure, PSL Research University, 75005 Paris, France. ✉email: udist@volcani.agri.gov.il

of the presence of mesoscale SST patterns on the atmospheric circulation and the resulting precipitation. The general methodology used in this study follows previous studies by comparing a control simulation with other sensitivity simulations in which small-scale ocean dynamic is removed ([14,15,38]). Here, the mesoscale SST anomaly impact is demonstrated for one specific cyclone in the MS using coupled and uncoupled simulations at 5 km resolution both in the atmosphere and the ocean. The comparable high resolution, together with a high-frequency atmosphere-ocean exchange of properties (10 seconds), allow for resolving the dynamical mechanism both spatially and temporally. Similar modeling studies investigating the role of SST have been performed in the MS by[3,4,6,11]. This study further extends these studies by focusing on the mesoscale SST variability in the January 2020 flood event.

The following section briefly describes the atmospheric conditions that led to the heavy rains. Section 3 presents results from different numerical simulations designed to emphasize the impact of mesoscale eddies through air-sea interactions on the atmosphere. Section 4 discusses the dynamical processes involved in these interactions on the resulting weather. A conclusion is offered in the last section.

The January 8-10, 2020 floods

On January 8-10, 2020, severe floods occurred over Israel's northern and southern coastal plain, between the seashore and the mountains, 20 km inland, further east. The most severe floods took place up to the drainage channel of Nahal Hagaton, where the city of Naharia resides. The observed rainfall over the region reached $\sim$ 150 mm. Such an amount, which constitutes about 15% to 25% of the annual rainfall in this region, fell in just two days. One person lost his life during this event, and heavy damage to private property and infrastructure was reported. The municipality of Naharia city, for example, estimated damage to the infrastructure of about 20M US dollars, excluding loss of private property.

About 36 hours before the beginning of the floods (January 6), a cutoff low ($\sim$1500 km size) was located over the Aegean Sea, accompanied by a surface low, with the same size and location (Fig. 1a). A first phase of high precipitations occurred at that time over Southern Turkey. The SST anomaly (with respect to a $300\ \mathrm{km}^2$ box mean) field in the MS on January 6 displayed high mesoscale ($\leq$100 km size) activity, reaching 1°C within 20 km (Fig. 1b). Particularly relevant to this study, the Eastern MS was characterized by warm and cold mesoscale SST anomalies north of Egypt.

In the following 36 hours, the cyclone moved eastward, crossing the warm SST anomalies in the Eastern MS (Fig. 1b). At that time, a second phase of heavy rains affected the Levant (eastern Egypt, Sinai Peninsula, Israel, Jordan, Lebanon, and Syria). For Israel, this phase can be further split into two parts: on January 8, most of the precipitation was concentrated over the northern part of Israel, and on January 9, precipitation occurred mostly over its southern coastal plain. This explains the bimodal distribution revealed by the Israeli Meteorological Service (IMS) observations (Fig. 2a): large amounts were observed in the northern and the southern coastal plains relative to its central part. Integrated Multi-satellite Retrievals for GPM (IMERG) observations (Fig. 2b) confirm this bimodal shape and further reveal a northern precipitation peak extending to Lebanon and Syria and other peaks north and west of Cyprus.

We found that MS has experienced a long-term warming trend in recent decades (SI Figure 1), and specifically at the time of storm development (SI Figure 2). A recent study has also indicated an increase in precipitation in Israel during the past decades, attributed to changes in SST and an increase in rain intensity per rain event (yet a decrease in the total number of events)[39]. These factors could have a general positive contribution to the cyclone intensity. Because of the well-known impact of mesoscale SST anomalies and related SST gradients on moisture fluxes through air-sea interface[40,41], the question we would like to answer here is to what extent small-scale SST anomalies and gradients can explain the precipitation distribution observed over the coast of Israel.

Simulation's results

We have designed a set of numerical simulations to study the dynamical processes explaining the observed precipitation patterns (see Methods). Briefly, this set includes three major simulations initialized on January 1 and integrated for nine days until January 10, using the same initial and lateral boundary conditions: (i) CPL, a regional coupled simulation, initialized with the ERA5 atmosphere and HYCOM ocean reanalysis datasets; (ii) ATM, an equivalent atmosphere-only simulation forced by SST (from CPL simulation, zero currents), updated every six hours; (iii) SMT, a smoothed atmosphere-only simulation, similar to ATM, except that the SST field is smoothed using a boxcar filter of 1° by 1° (see Figure S2, which illustrates the SST difference between ATM and SMT, and see also the Methods section for more information about additional simulations performed to estimate the uncertainty of the results). All simulations used the same atmospheric boundary conditions from ERA5.

The CPL simulation reveals a conspicuous pattern in the field of Total Column Precipitable Water (TCPW) (Fig. 3a) over the Eastern MS on January 7. This pattern is associated with a meso-cyclone ($\sim$300–400 km size), located at 30°E longitude in the westerly wind sector south of the synoptic-scale cyclone. Later on, the TCPW pattern propagates eastward and intensifies, possibly gaining moisture (Fig. 3b) from warm SST anomalies (SI Figure 3). Then, TCPW quickly decreases over land, due to the rain. This sharp evolution of the mesoscale TCPW pattern implies that the warm mesoscale SST anomalies in the Eastern MS may have controlled the moisture supply into it and affected its intensity. This TCPW pattern is consistent with a large increase in latent heat flux (SI Figure 4) associated with the crossing of the meso-cyclone over the warm SST anomalies.

Figure 4 displays the precipitation from the three simulations: (i) CPL (Fig. 4a), (ii) ATM (Fig. 4b), and (iii) SMT (Fig. 4c). Of the three simulations, the CPL simulation shows the best agreement with observations in terms of precipitation amounts and its spatial distribution (Fig. 6). The CPL simulation (Fig. 4a) is able to reproduce the bimodal pattern and its intensity, though the central coast of Israel seems to receive more rainfall

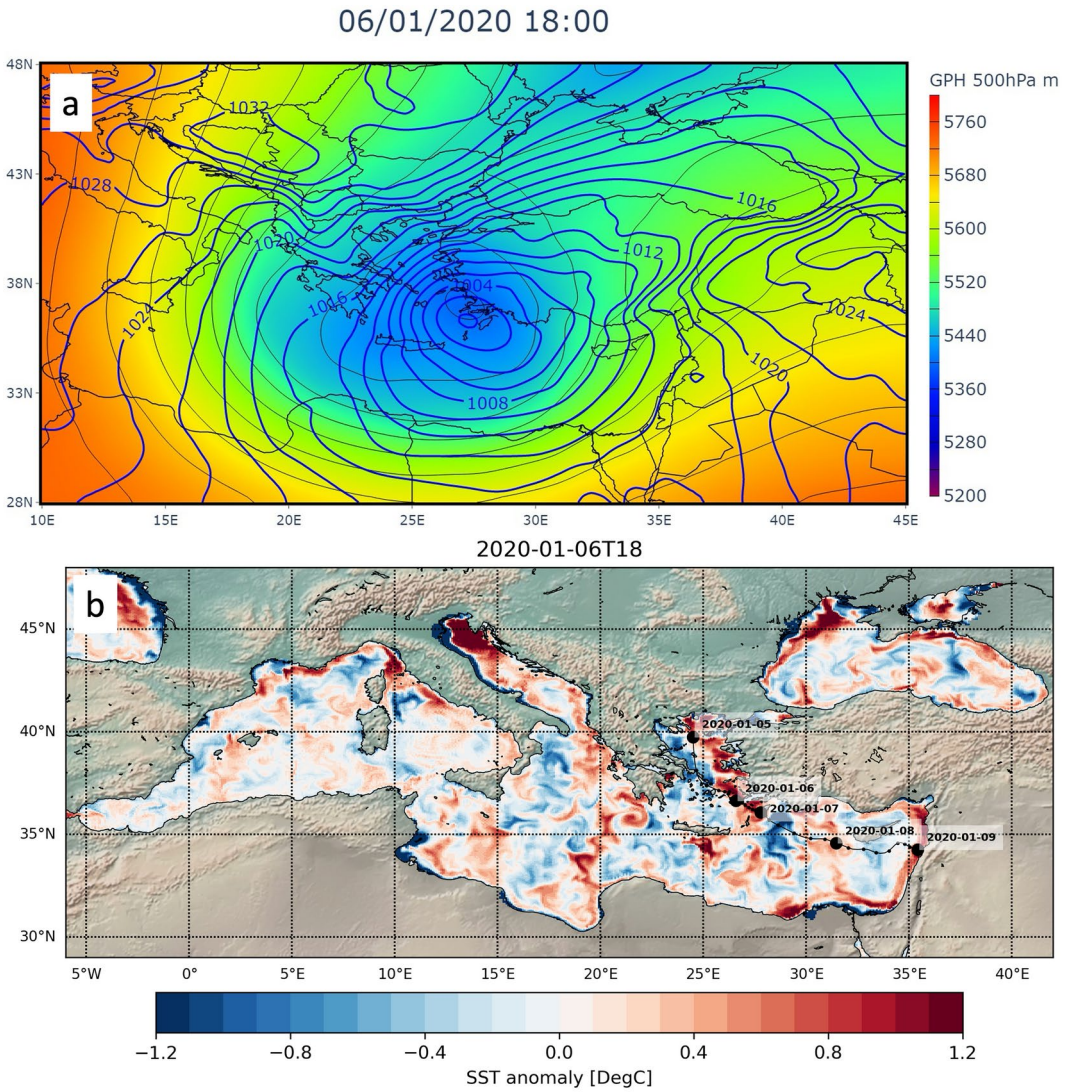

Fig. 1. (**a**) ERA5 reanalysis 500 hPa height (shading and gray contours) and surface pressure (blue contours) height (**b**) HYCOM reanalysis SST anomaly (with respect to $300\,\mathrm{km}^2$ box mean) and superimposed cyclone track. Both fields are shown 36 hours before the beginning of the floods.

than observed. The ATM simulation (Fig. 4b) generates less precipitation than CPL, whereas the SMT simulation (Fig. 4c) increases precipitation relative to ATM but it smears the precipitation patterns over a larger area than the ATM. Particularly, it increases precipitation over Turkey, where precipitation was not observed. Figure 5 confirms that ATM and SMT simulations display less precipitation than CPL over central Israel, with a deficit of almost 50% of the total precipitations. Here CPL-ATM represents the effect of coupling, CPL-SMT represents the effect of coupling plus SST resolution, and ATM-SMT is the effect of SST resolution. CPL has higher rainfall amounts in the south and north, and lower rainfall amounts in the center, as expected from observations. The rainfall in the north and west of Cyprus is also captured by the CPL, not precisely in the right location, but with a magnitude similar to observations. The rain in these regions is not well represented in ATM and SMT. The northern pattern in ATM and SMT seems to be shifted to southern Turkey.

The TCPW field over Israel resembles dipole/quadrupole patterns, undergoing a space/time shift that differs between the various simulations. In the CPL, the meso-cyclone associated with TCPW (Fig. 3) propagates slightly faster than in the ATM simulation, as indicated by the red pattern in the eastern part of the meso-cyclone (Fig. 7a,c,e). The SMT simulation does not seem to change its propagation relative to ATM, but rather its rotational speed (Fig. 7b,d,f). The CPL simulation further indicates that the TCPW pattern and its associated precipitation arrived at the Eastern MS shore on January 8, entering the northern coast of Israel in the morning hours (Fig. 8a). A day later, a narrow TCPW train is observed to enter Israel's southern coastal plain, leading to enhanced precipitation (Fig. 8b). These two rain episodes, in North and South Israel, left minimum in the central coastal plain, as found in observations (Fig. 2). In the ATM simulation, the mesoscale TCPW pattern approaches Israel at the North (Fig. 8c). However, because the TCPW train is wider (Fig. 8d), the total precipitation pattern spreads across Israel's coastal plain. In SMT, the mesoscale TCPW pattern spreads across Israel's coastal plain

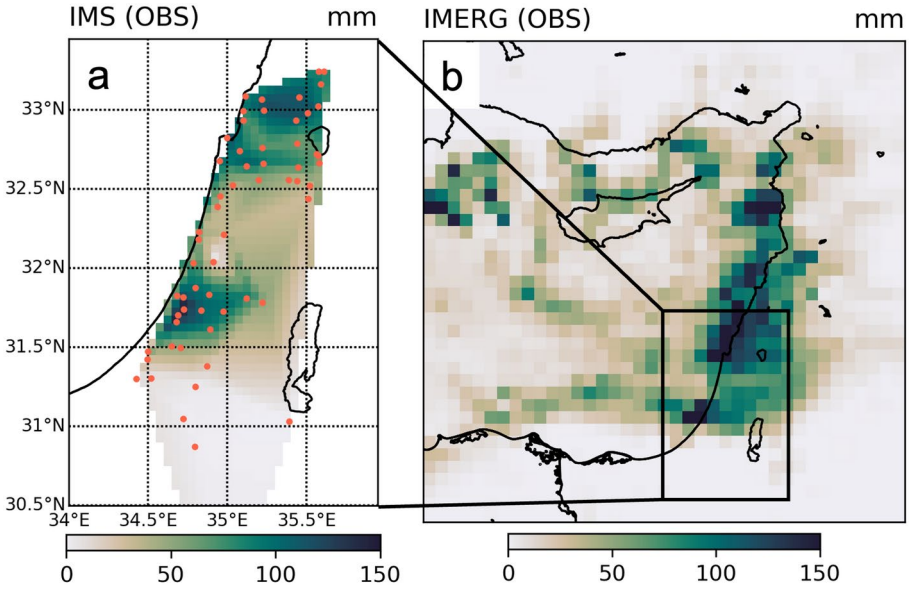

Fig. 2. Accumulated precipitation 8-10, January based on (**a**) interpolated in-situ observations - red dots represent available observations, and (**b**) IMERG. In Israel, a bimodal distribution is observed along the coastal plain. The northern rainfall peak extends to the north (Syria and Lebanon). Two more precipitation regimes are found in the north and west of Cyprus.

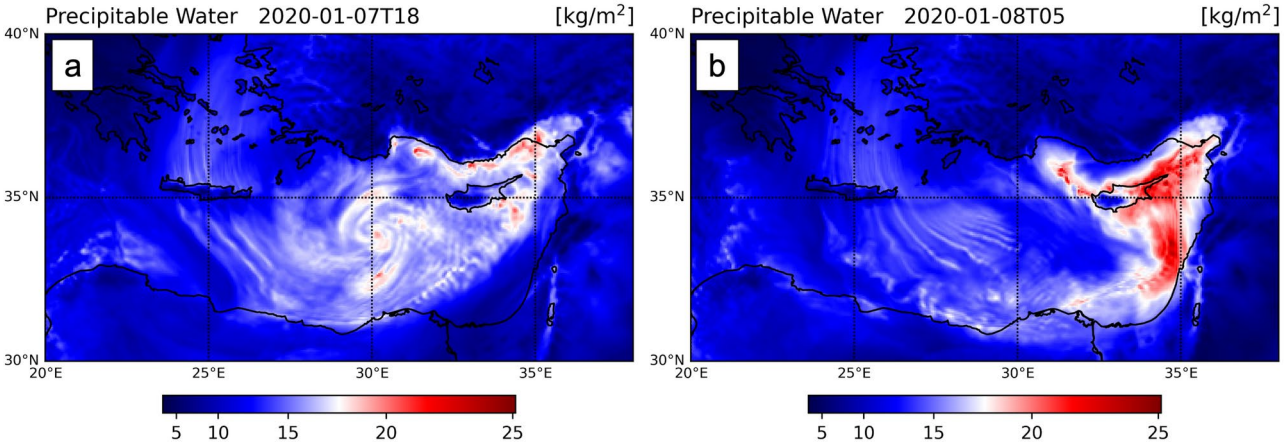

Fig. 3. Total Column Precipitable Water (TCPW) before and after the passage above the warm mesoscale eddies at the Eastern MS from the CPL simulation. TCPW includes both liquid water and water vapor.

(Fig. 8e), and the TCPW train is even wider and located more to the North relative to CPL and ATM (Fig. 8f). This indicates that ATM failed to represent the TCPW train while SMT failed to represent both the mesoscale TCPW and the train.

To study the uncertainty of the results, we performed additional four ATM and four SMT simulations in parallel (a total of five ATM and five SMT simulations). They were forced by the same SST boundary conditions but initialized on different days. These experiments, together with the core experiments, are equivalent to five ATM or SMT simulations initialized on the same day using different initial conditions but sharing the same lower and lateral boundary conditions. We have not performed additional four CPL simulations because that would have resulted in five different SST fields. Having five CPL simulations could mask the initial condition uncertainty (or the "irreducible" uncertainty) by generating five SST fields, thus, adding another source of uncertainty (due to different SST). The ensemble-based difference plots (SI Figure 5) further confirm that the improved results of the CPL with respect to ATM and SMT are not related to initial condition uncertainty. The ATM-SMT figure (Fig. 5c) indicates that increasing the SST resolution also contributes to generating the bimodal pattern in the ATM simulation but is not as good as in the CPL one.

From these results, the fully coupled simulation (CPL) performs better than atmosphere-only simulations (ATM and SMT), and in particular, better than the ATM simulation that has the same initial conditions, and

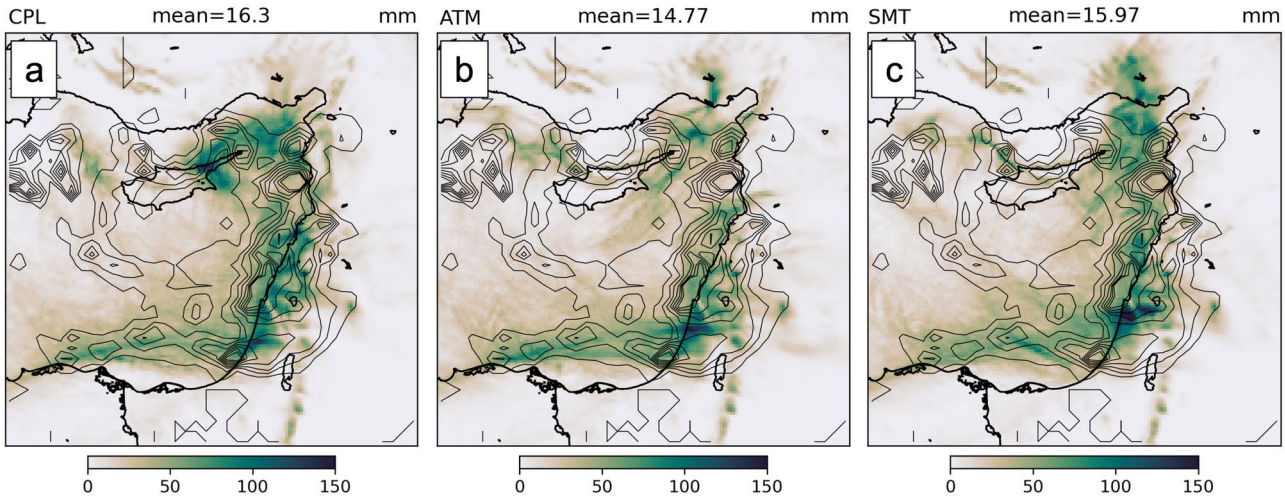

Fig. 4. Accumulated precipitation 8-10, January for (**a**) CPL, (**b**) ATM, and (**c**) SMT. Observed IMERG precipitation is depicted in contour lines (20 mm contours).

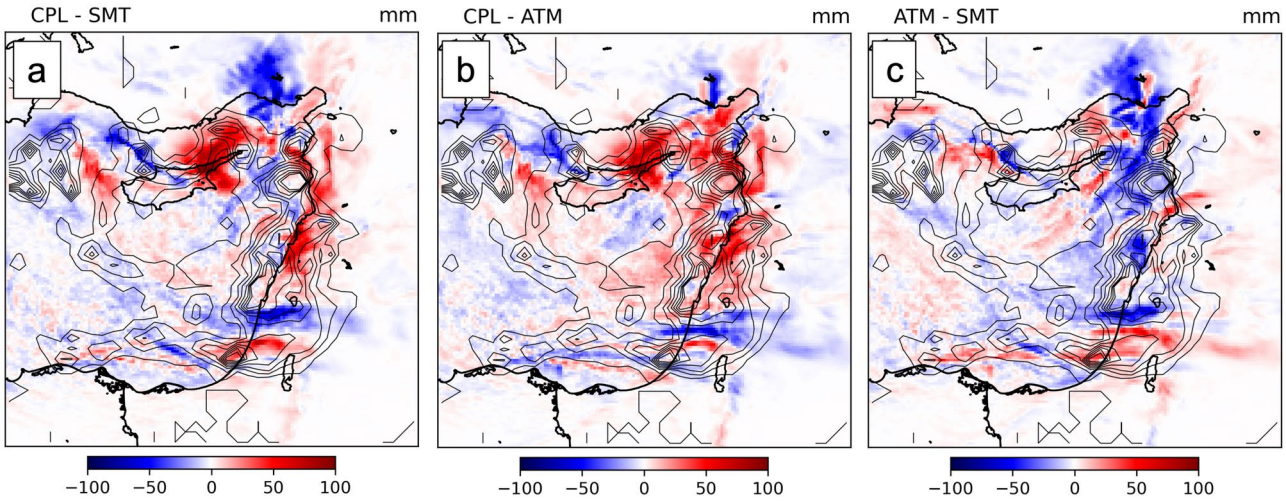

Fig. 5. Total precipitation differences between experiments are shown for (**a**) CPL - SMT, (**b**) CPL - ATM, and (**c**) ATM - SMT. Observed IMERG precipitation is depicted in contour lines (20 mm contours). The coupled simulation consistently pushes the model results toward observed values.

for which the SST field is exactly the same as in CPL. Thus, CPL increases the rainfall along the coastal region of Syria, Lebanon, North Israel, in agreement with IMERG observations, however, with some apparent shift to the East relative to IMERG. CPL is also able to reproduce the precipitation patterns to the North and west of Cyprus. In ATM, the peak of precipitations to the North of Cyprus was shifted further to the North, towards south Turkey, and the peak of precipitations west of Cyprus is considerably underestimated.

This first analysis strongly suggests that the rainfall over the coast of Israel reflects interactions between dynamical processes associated with features of different scales: (i) air-sea moisture fluxes, involving mesoscale MS SST anomalies (10–200 km), (ii) a lower-tropospheric meso-cyclone (<500 km) with a strong signature in the TCPW field, and (iii) an upper-tropospheric synoptic cyclone (1500 km). The following section further analyses these dynamical processes.

Understanding the dynamical processes

Surface winds can shed some light on the mechanisms controlling the differences among the simulations. Figure 9 reflects considerable surface wind difference between CPL and ATM, with CPL having stronger eastward winds, but smaller westward winds to the north (near Cyprus). The difference between the wind speeds can be attributed to a shift of the meso-cyclone to the North-East. Results from ATM and SMT simulations are close, and in particular, the location and strength of the meso-cyclone are similar. The main difference is that the

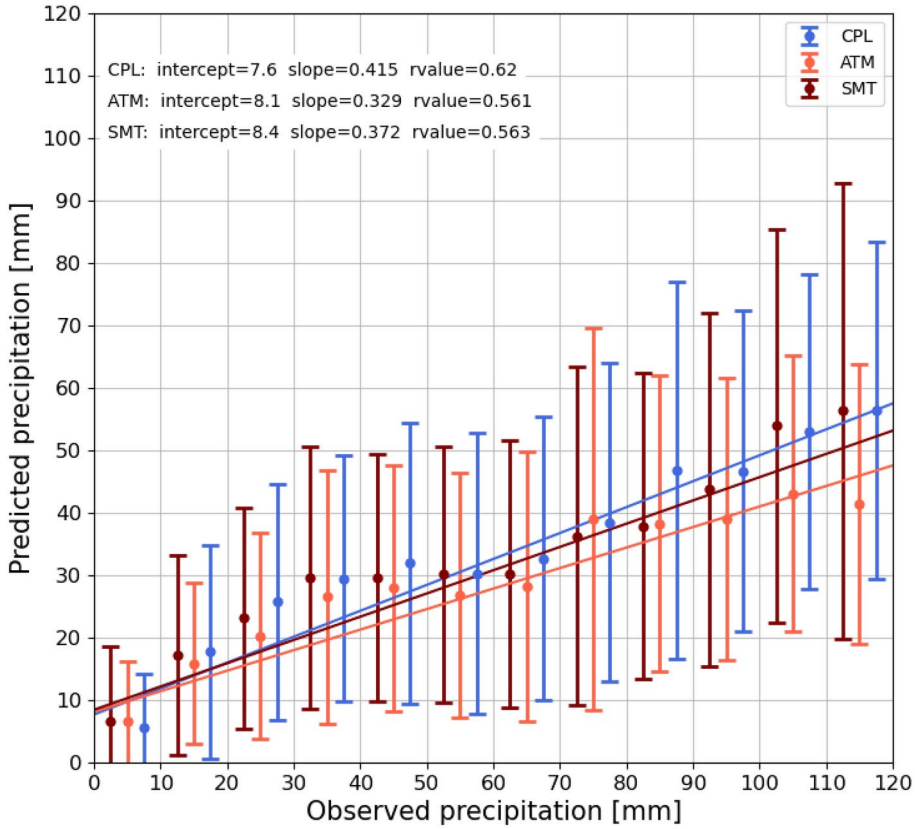

Fig. 6. Binscatter plot (mean in markers and standard deviation in error bars) and regression lines for CPL, ATM and SMT. CPL has a significantly better slope (closer to one) and a better correlation relative to ATM and SMT.

rotation around the cyclone center has changed (positive and pointing to the East, south of the cyclone center; negative and pointing to the West, North of the cyclone center).

Two main contributors to the surface wind speed differences between simulations may be suggested – wind stress and pressure gradients (see methods for more information). These two are plotted in Fig. 9c-f. The source for the change in surface winds seems to come mostly from changes in wind stress (Figure 9c,d). The change in wind stress suggests the involvement of the downward momentum mixing (DMM) mechanism[42] (see also SI Figure 6). Likewise, the changes in pressure gradients may be associated with the pressure adjustment (PA) mechanism[43]. The increase in surface winds in CPL relative to ATM and the faster rotation in ATM relative to SMT are both highly correlated with the wind stress, suggesting that these mechanisms contribute to the precipitation in CPL. Pressure gradient (Fig. 9e,f) also seems to play an important role, but to a lesser extent. Positive and negative anomalies are found below the meso-cyclone location but the pattern is less correlated with the surface wind pattern. The anomaly pattern of the pressure contribution may indicate its contribution to the northward shift of CPL relative to ATM and the faster rotation of ATM relative to SMT. SI Figure 7 further indicates the significance of the DMM and PA mechanism based on a new recently developed metric[44]. Here, DMM and PA mechanisms were found to be significant only on the days before the storm.

To further understand why CPL performs better than ATM and SMT in terms of TCPW and precipitations, we analyzed additional simulations emphasizing the characteristics of the ocean variables that impact the atmosphere. First, we analyzed the sensitivity of the atmosphere to the frequency of these variables, particularly the frequency of SST and ocean currents updates. The first additional simulation is the FREQ simulation, which is similar to ATM, except for the SST forcing taken every hour instead of 6 hours. The difference between FREQ and ATM in terms of wind stress and TCPW reveals a significant northward displacement of the meso-cyclone by the FREQ (Fig. 10e, f), which is closer to the CPL. This suggests that air-sea moisture fluxes are sensitive to the frequency of the SST forcing that may differ in northern and southern parts of eastern MS. The second additional simulation, FCUR, is similar to FREQ, except for the inclusion of surface currents in the surface boundary conditions every hour (instead of zero current in FREQ). The differences between FCUR and FREQ (Fig. 10c,d) are again significant, in particular in the center of eastern MS, suggesting that the surface currents in this region cannot be ignored when considering TCPW. It was found that the cyclone location in FREQ was to the west of FCUR (SI Figure 8). This difference may suggest that the alignment of currents to the wind could reduce surface wind stress and increase the cyclone's translational speed. At last, FCUR may be considered similar to CPL, except for the forcing, taken every hour instead of every 10 seconds in CPL. Results again indicate a significant difference between the CPL and FCUR simulations in terms of TC PW (Fig. 10a, b). These results indicate that

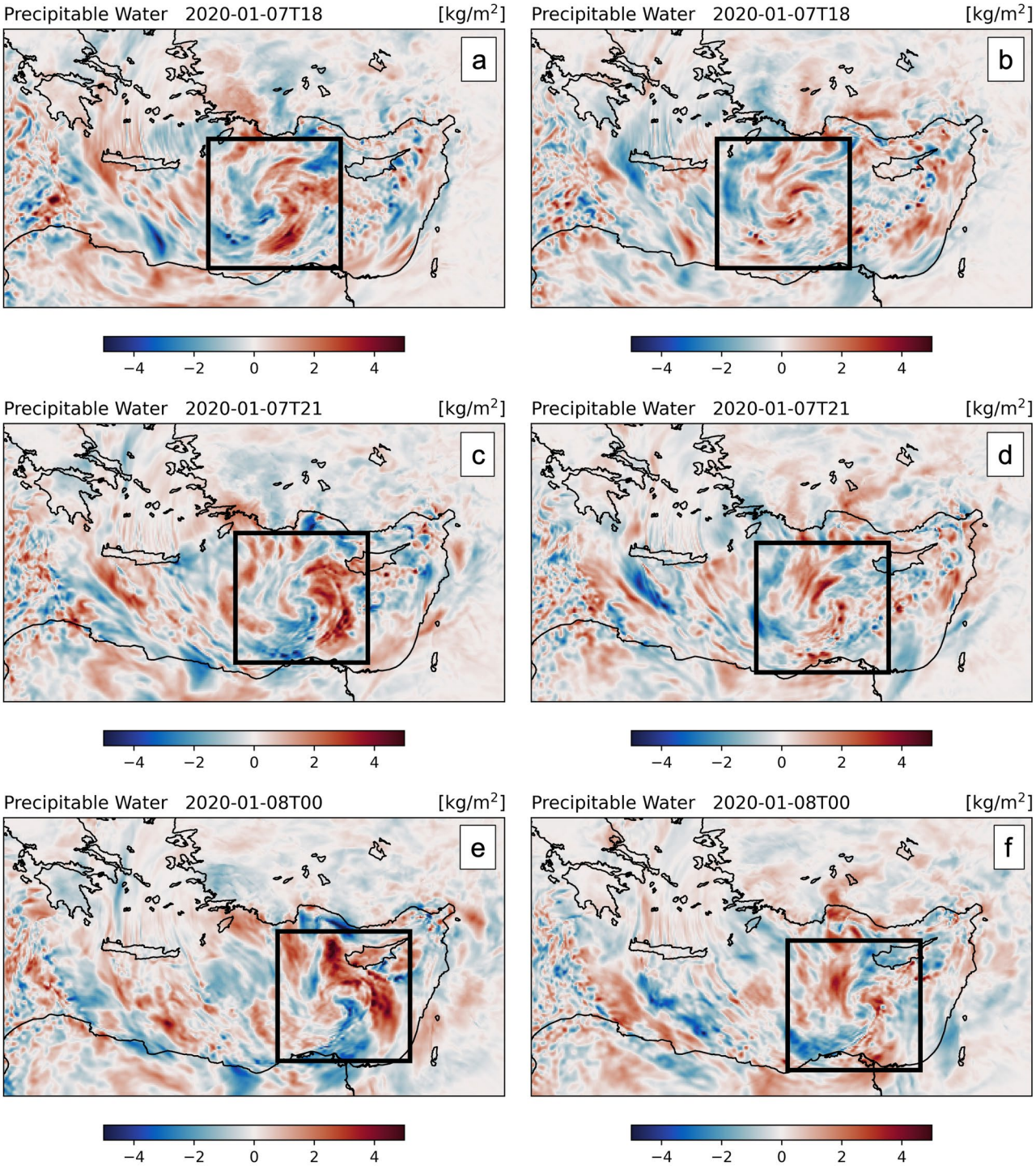

Fig. 7. TCPW difference CPL-ATM (**a,c,e**) and ATM-SMT (**b,d,f**) for three dates. The black rectangle approximates the location of the mesoscale cyclone.

the main advantage of the coupling comes from the inclusion of currents when comparing the pattern of the difference in Fig. 8 with Fig. 10c.

In summary, mesoscale sea eddies, through their associated SST anomalies, directly impact surface latent heat (moisture) fluxes because of the SST gradients at the eddy edges. This explains the difference between ATM and SMT. As emphasized by Frenger et al. (2013)[17], because of the strong SST gradients at the eddy edges, the atmosphere is destabilized above warm eddies, which brings momentum from upper levels, which leads to an increase in surface winds above warm eddies and, therefore, increasing turbulence and latent heat fluxes. The opposite holds above cold eddies. However, because of the asymmetric response of warm and cold eddies, sea eddies lead to a net moisture release to the atmosphere[45–47]. The differences between FREQ and FCUR reflect

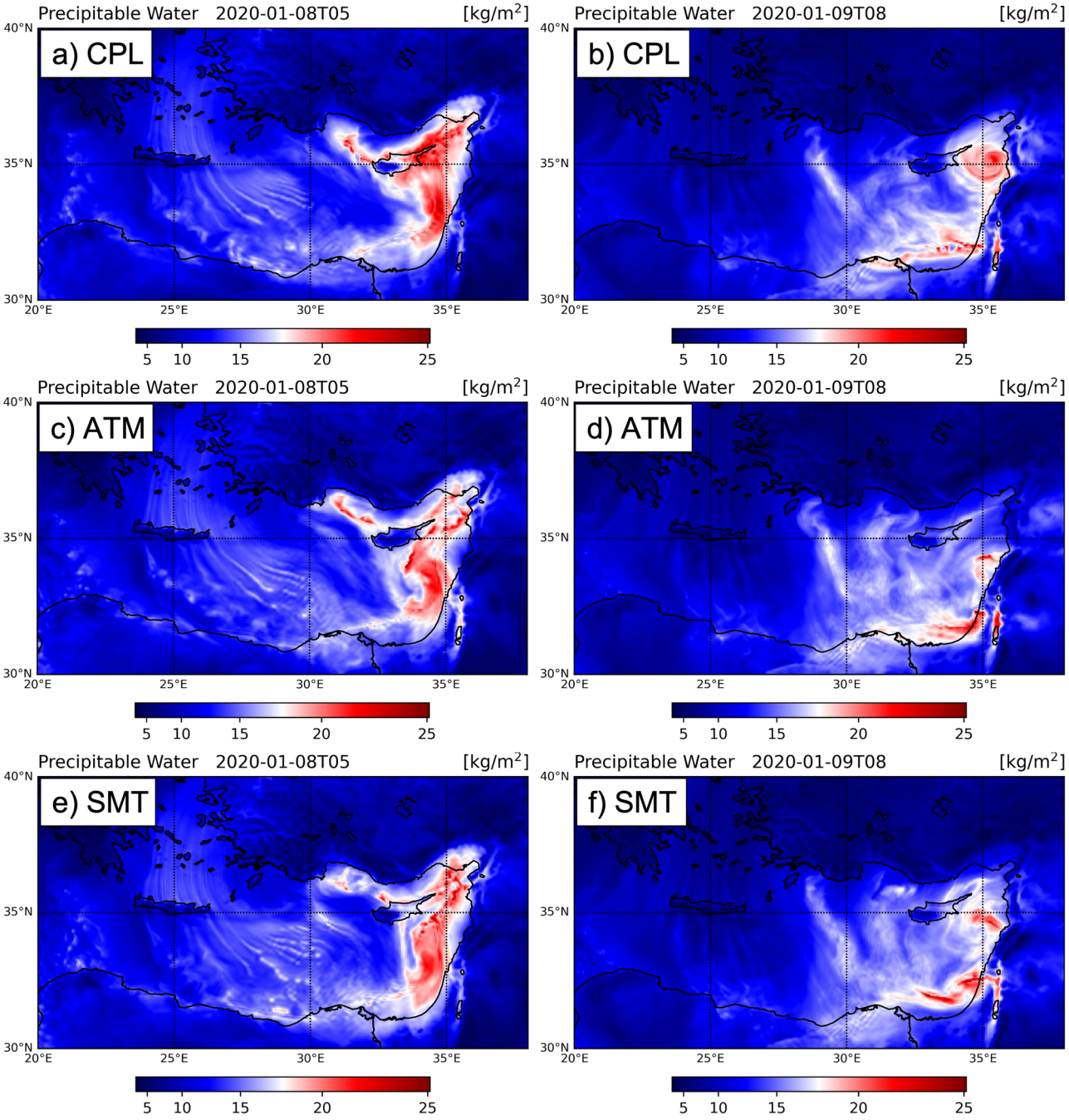

Fig. 8. Total column precipitable water at the beginning of the first (**a-c**) and the second (**d-f**) precipitation phase for CPL (**a,d**), ATM (**b,e**) and SMT (**c,f**).

the impact of surface currents forcing. One possible explanation is the well-known impact of surface currents on wind stress and, in particular, of surface currents associated with mesoscale sea eddies on the wind stress curl and divergence[48,49]. Such wind stress curl and divergence are known to affect the atmospheric weather[23]. Thus, the results from the three major simulations (CPL, ATM, and SMT) and the additional simulations (FREQ and FCUR) confirm the impact of mesoscale sea eddies on the TCPW and the resulting precipitations over the west coast of Israel. The differences between CPL and FCUR are more puzzling. In both simulations, the atmosphere has the same boundary conditions at the air-sea interface, except for the frequency: ocean variables are taken every hour in FCUR instead of every 10 seconds in CPL. The meso-cyclone mentioned above is a feature confined to the lower levels of the troposphere (SI Figure 9) and is apparently generated above the Mediterranean Sea. It may be produced by the instability of the upper-tropospheric synoptic system, with positive relative vorticity much larger than the Coriolis parameter f (SI Figure 9). Large wind stress curl and/or

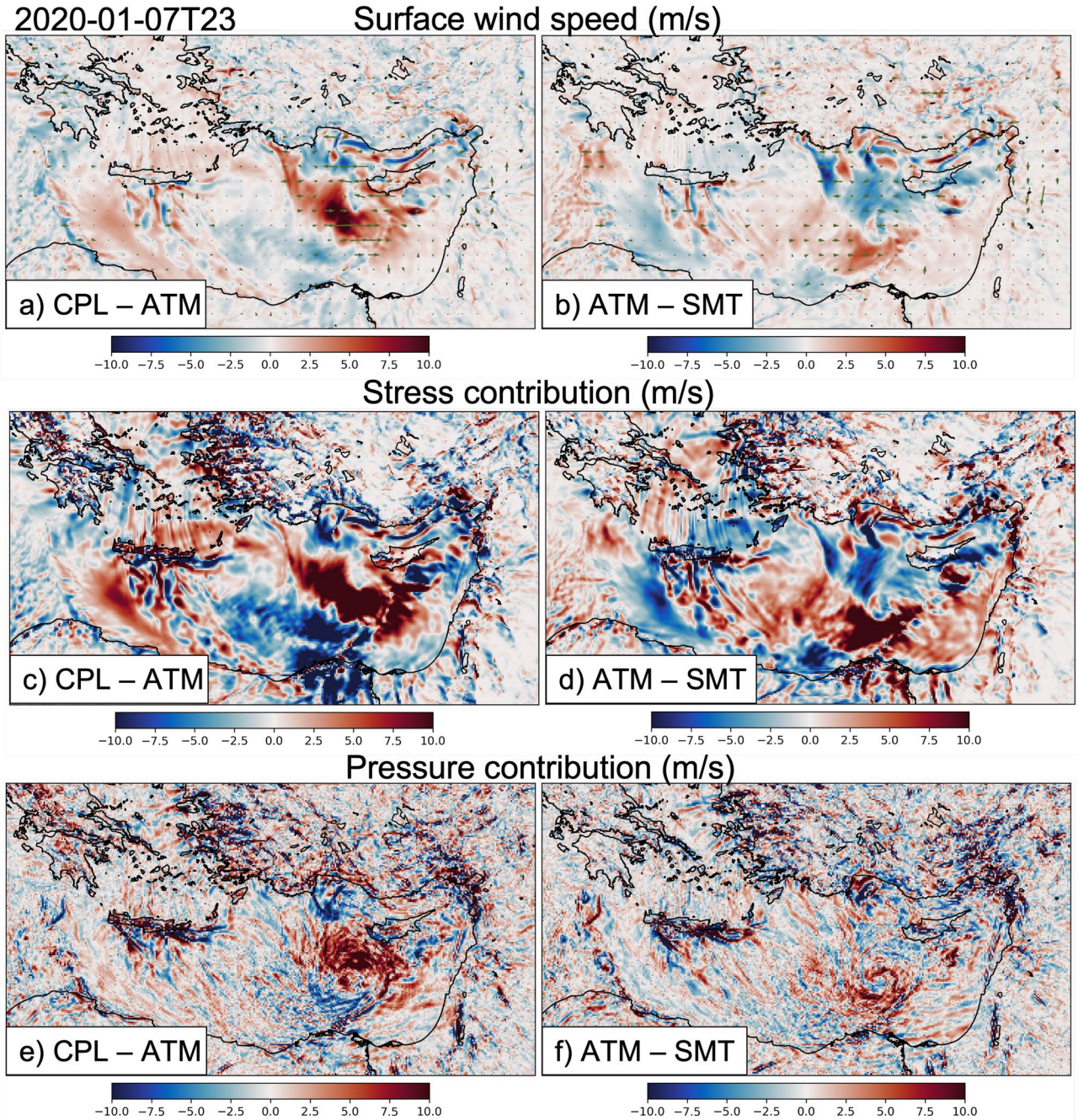

Fig. 9. (**a,b**) One snapshot (2020-01-07 23:00) of surface wind difference; (**c,d**) stress contribution to the wind speed equation; (**e,f**) pressure contribution to the wind speed equation for CPL-ATM (**a,c,e**) and ATM-SMT (**b,d,f**). Green arrows in Panels a-b represent the difference in surface winds.

divergence values associated with sea eddies at the air-sea interface can easily destabilize such fronts, producing intensified meso-cyclones. This is something to be investigated in a future study.

Discussion and conclusion

Our results suggest that air-sea interaction and mesoscale SST variability may have a crucial role in determining the spatial distribution of rainfall. This was demonstrated by performing a set of modeling sensitivity experiments using coupled and uncoupled simulations and using various SST fields in the uncoupled simulations. In particular, we found a direct impact of coupling and SST variability on the moisture flux from the MS, which resulted in higher TCPW in CPL relative to ATM and in ATM relative to SMT at the core of the cyclone that later precipitated over land.

This study investigates the impact of sea mesoscale eddies on the atmosphere and the potential influence on the January 2020 flood event that occurred in Israel. Since the meso-cyclone is represented in all of our sensitivity

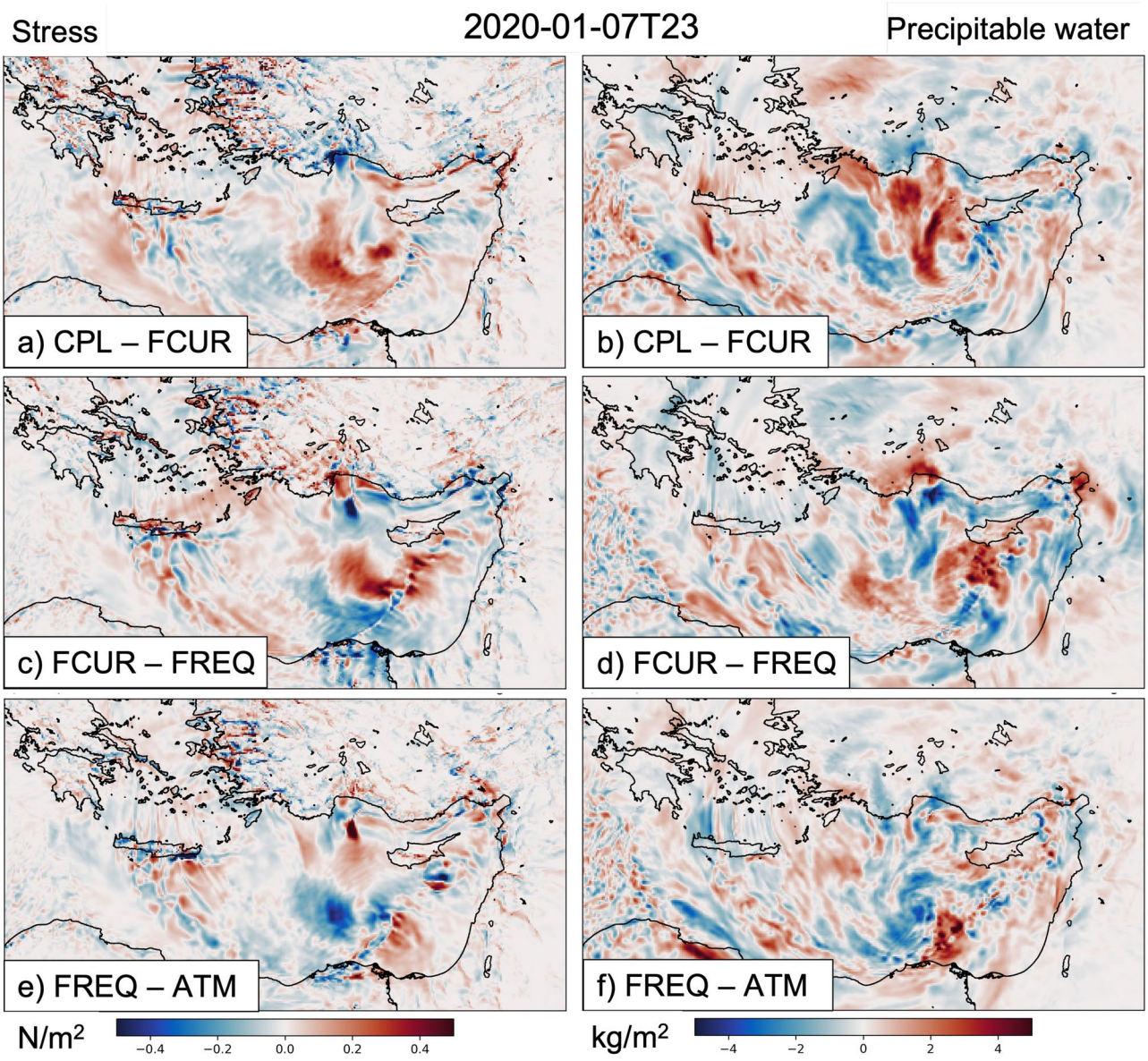

Fig. 10. Wind stress (left) and TCPW (right) differences between simulations for (**a,b**) CPL - FCUR, (**c,d**) FCUR - FREQ, and (**e,f**) FREQ - ATM. Jan 7, 11 PM, 2020.

experiments, it suggests the factors we tested (e.g., coupling, SST variability) are not responsible for the genesis of the cyclone. Also, our study does not indicate that the water vapor source for the cyclone is local. Yet, this study indicates that the inclusion of small-scale ocean dynamics in a coupled sea-atmosphere model, as well as high-frequency air-sea coupling, have an important role in increasing the model performance to reproduce this event. Both sea surface currents and SST play an important role.

It is important to note that all the static fields in our simulations are kept constant (terrain, land use categories, soil categories, etc,...). Except for the changes described in the text (e.g., coupling, SST variability, currents), all other properties in the simulations are the same. Therefore, although one can, for example, attribute the change in precipitation to the change in the location of the cyclone (e.g., in FCUR relative to FREQ), the source of the change in the model comes from the change in the forcings (the inclusion of currents in the case of FCUR relative to FREQ).

Figure 9 suggests that DMM is the governing mechanism in regulating surface winds. However, unlike the classical wind change above SST anomalies, here, the change in wind propagates along the meso-cyclone, and does not remain stationary above the eddies. Nevertheless, air-sea coupling and SST resolution considerably control the degree of agreement between the simulations and observations. It turns out that air-sea coupling and SST resolution initiate the anomalies through changes in vertical mixing, but once they are initiated, the anomalies propagate with the meso-cyclone.

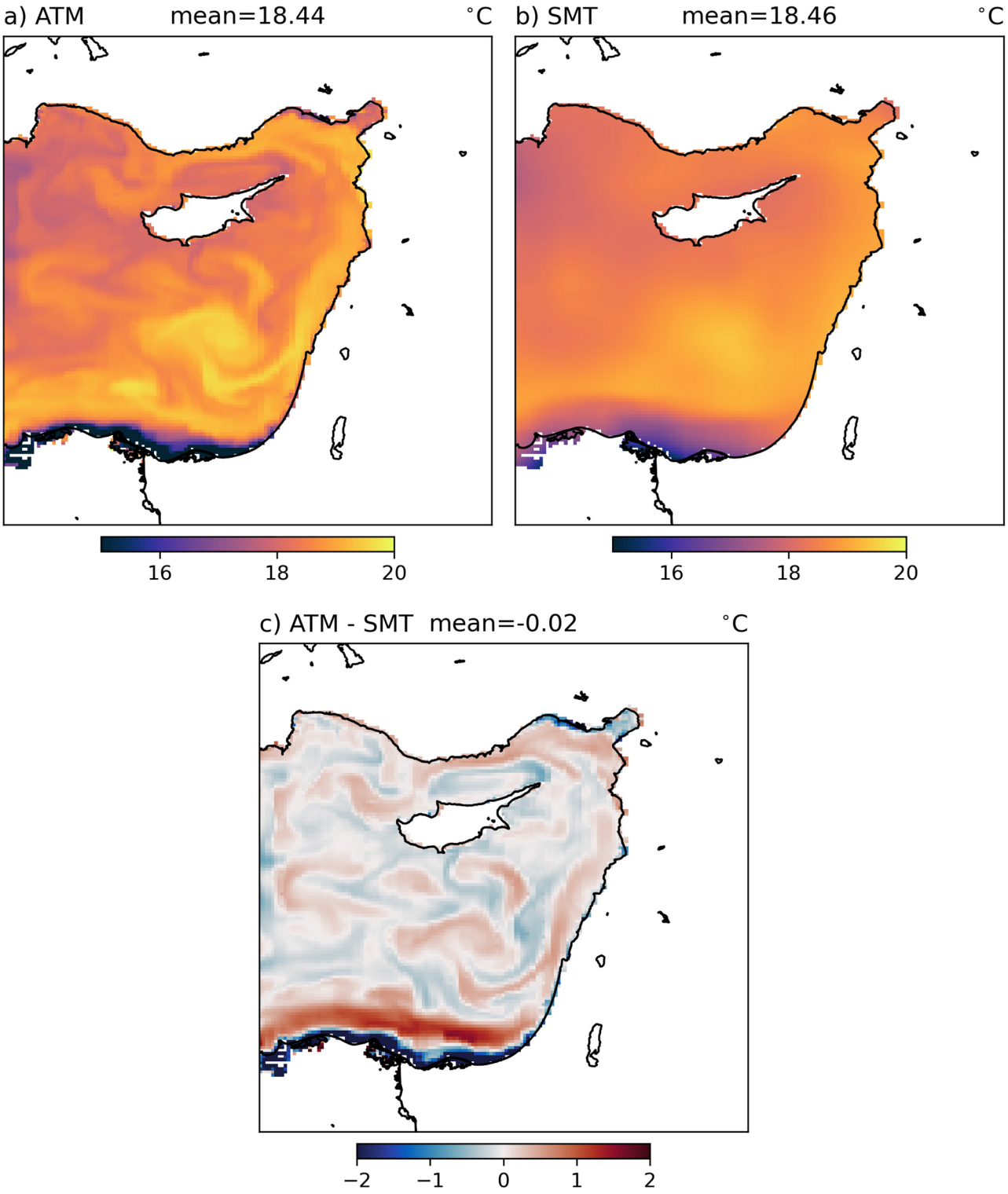

Fig. 11. SST snapshot from ATM (**a**) SMT (**b**) and their difference (**c**) at 2020-01-08T06.

Wind speed and wind stress differences between the CPL and ATM simulations seem to be mostly related to the effect of sea currents. This finding is explained by the high spatial correlation between Fig. 9a and Fig. 10c, indicating that the simulation with current (FCUR) relative to the one without current (FREQ) reflects the difference pattern. Unexpectedly, we also find notable differences between CPL (coupled) and FCUR (uncoupled, one-hour forcing). Here, both simulations have currents, and one may think that a one-hour resolution of forcing for the ocean may suffice to represent coupling mechanisms in the slow-evolving ocean. However, the difference between CPL and FCUR is not only the coupling frequency since the ocean state in FCUR is one that

was developed by interacting with the atmosphere every ten seconds (CPL SST and currents). The difference between CPL and FCUR is, therefore, also related to sub-hourly air-sea interactions.

Yet, at this stage, we do not have a good explanation for the large difference in wind stress between CPL and FCUR (Fig. 10a). A rough estimation of the difference between CPL and FCUR stresses indicates a small effect. As an example, if we consider an idealized setup, 1 Pascal wind stress applied on a 100m ocean mixed layer with a zero-current will result in 3.6 cm/s current in one hour ($\frac{1[Pa]}{1000[kg/m^3]\cdot 100[m]}\cdot 3600[s/h] = 0.036m/s$). In FCUR, this feedback is inactive: the ocean will not respond, and currents will not change their velocities. A difference of $0.036m/s$ between the two cases (with and without feedback) does not explain a change of about $0.2Pa$ found in Fig. 10a. Nevertheless, small differences may accumulate over time, and if they propagate with the mesoscale pattern, they may explain the simulated differences.

One major result of this study is that the January 2020 flood event is principally explained by the formation of a lower-tropospheric meso-cyclone over the Mediterranean Sea that takes moisture from the sea, subsequently triggering heavy precipitation when mesoscale air currents are pushed inland, over the mountainous coast of Israel. Characteristics of this meso-cyclone are susceptible to the coupling mechanisms at the air-sea interface: High-resolution SST anomalies significantly impact the meso-cyclone TCPW. Sea surface currents, as well as the frequency of the air-sea coupling, have a substantial impact on TCPW as well. The lower-tropospheric meso-cyclone has a size of ∼300–400 km, intermediate between the synoptic-scale cyclone, ∼1500 km size, and MS eddies, less than ∼100 km in size. As such, it is more sensitive to air-sea coupling at scales of the order of 100 km than the synoptic cyclone. One question still needs to be addressed is how this meso-cyclone is formed. In particular, whether this is due to the instability of fronts associated with the synoptic-scale cyclone or forced by the air-sea coupling involving Mediterranean Sea eddies.

Two other conclusions can be drawn from the above study. One is that anomalies in the Eastern MS have a crucial contribution to the distribution of rain over the region, including the Levant. Second, the WRF model is capable of reproducing this effect when the air-sea coupling is introduced.

Methods

The CPL simulations

The CPL simulations were performed using the Scripps-KAUST Regional Integrated Prediction System (SKRIPS) model, which is constructed from the Weather Research and Forecasting (WRF) atmospheric model coupled to the Massachusetts Institute of Technology general circulation model (MITgcm) ocean model[50]. The model domain is shown in SI Figure 10. WRF was configured with the Single-Moment 3-class microphysics scheme, Kain-Fritsch Cumulus parameterization, RRTMG for long and short-wave radiation, the Monin-Obokhov based surface layer scheme, and the Yonsei University PBL scheme. Gasper et al. (1990)[51] vertical mixing scheme was used in MITgcm.

Three CPL simulations were conducted. They were initialised on Jan 1, Jan 2, and Jan 3, 2020, and integrated until Jan 10, 2020. The atmospheric initial and boundary conditions were taken from ERA5 reanalysis[52] and the oceanic initial and boundary ocean conditions were taken from HYbrid Coordinate Ocean Model (HYCOM) analysis[53]. SST and sea surface currents from MITgcm are exchanged with the atmospheric model and used to calculate air-sea fluxes that are updated at every model time step (10 seconds for the atmosphere and the ocean). Boundary conditions in the atmosphere and the ocean were updated every six hours. WRF horizontal resolution was 0.05° by 0.05° (about 5km horizontal resolution) with 39 vertical levels. MITgcm horizontal resolution was the same as WRF (sharing the same horizontal grid) and it also had 39 vertical levels, starting at 2-meter thickness for each of the first six levels.

CPL simulations include three realizations but only one was used for the comparison with ATM simulations. This allowed us to assess the effect of the uncoupled simulations under the same SST conditions. The use of the three CPL simulations was only done to assess the uncertainty between the CPL simulations, which was found to be small (SI Figure 11). Arguably, the small difference between the simulations is not surprising considering the slow evolution of the SST fields for the integrated period (SI Figure 3). SI Figure 12 and SI Figure 13 compare the SST fields from the first CPL simulation with OISST and HYCOM. Not surprisingly, CPL has better agreement with HYCOM, since HYCOM's sea temperature on January 1 was used to initialize CPL.

Atmosphere-only simulation forced with observation-based SST

To increase our confidence in the CPL simulations, we have performed an additional atmosphere-only simulation, forced with observed SST (ATMO). In terms of the main precipitation patterns (SI Figure 14), the CPL simulation was better at reproducing the observed fields. Qualitatively, the atmosphere-only simulation forced by ERA5 SST resembles the ATM simulation forced by SST from the coupled simulation: i.e., peak precipitation in the center of Israel rather than split between the north and the south, unobserved precipitation pattern over Turkey, precipitation pattern over Eastern Cyprus and to the west of Cyprus similar to observations.

ATM and SMT simulations

ATM includes five realizations of atmosphere-only simulations initialized every day between the 1st and the 5th of January 2020. These simulations use initial and boundary conditions from ERA5, and the SST was provided by CPL (updated every six hours). The reason for using SST from CPL and not observed SST was to study the effect of coupling by keeping the SST close to the SST in the CPL simulation but disabling the effect of the atmosphere on the ocean. In between these six hours, SST is kept constant, and it does not respond to changes in the atmospheric conditions above. An additional change in ATM relative to CPL is that, like the common practice in atmosphere-only simulations, it assumes zero current (which is, in general, very small relative to winds). The role of surface currents is further investigated in the FREQ and FCUR experiments described below.

EXP	Coupled	SST update	Ens.	Description	Objective
CPL	Yes	10 s	3	Control simulation	-
ATM	No	6 h	5	a) Like CPL, no coupling, no currents; b) like SMT, no smoothing	a) Test the effect of coupling; b) test the effect of SST variability
SMT	No	6 h	5	Like ATM, no eddies	Test the effect of eddies
FCUR	No	1 h	1	Like CPL, no coupling	Test the effect of coupling
FREQ	No	1 h	1	a) Like FCUR, no currents; b) like ATM, one-hour SST update	a) Coupling; b) SST update frequency
ATMO	No	6 h	1	Like ATM, observed SST	CPL performance
CONST	No	6 h	1	Like ATM but with temporal and spatial mean SST from CPL	Large scale SST variability

Table 1. List of sensitivity experiments performed and used in this study.

Except for the duration of the simulations (five to nine days), the last five days of the five realizations differ only by the initial conditions. The boundary conditions for the five simulations are the same during the time the simulations overlap. SMT simulations are identical to the ATM set of simulations except that the SST was smoothed using a boxcar filter of 1° by 1° (see Fig. 11 for an illustration of the effect of the SST smoothing in one snapshot). It is noted that in our broad definition, mesoscale eddies are not just quasi-circular patterns. They can also be long and narrow, like those situated in the coastal regions. The high horizontal resolution (5km) simulation suggests that even corner coastal points will average a square of $50\,\mathrm{km}^2$. This means that it will include about 100 grid points. Since coastal points are relatively few and even these few points are averaged over 100 points, we believe that their effect is small.

An additional simulation (CONST) was performed in which SST variability over the entire MS was removed by averaging the SST field over the simulated period (spatial and temporal average). These simulations produced a considerably lower amount of rainfall, which may be attributed to the lower SST in eastern MS resulting from the averaging (in general the Eastern MS is warmer than the Western MS). The simulated rainfall from this simulation is shown in SI Figure 15.

Validation with ASCAT

SI Figure 16 and SI Figure 17 compare the simulated surface winds in CPL, ATM, and SMT (first realization) with ASCAT satellite observations in two different snapshots. Overall, the three simulations agree with the main wind pattern. While the difference in surface winds seems to be small, they affect the resulting precipitation pattern as can be seen in Fig. 5.

FREQ and FCUR simulations

Two additional experiments were performed to further analyze the effect of forcing frequency and sea surface currents. FREQ simulation (only one initialized on January 1, 2020) is identical to ATM, except that the SST update happens every hour (SST is kept constant in between) instead of every six hours. Therefore, it can demonstrate the effect of SST update frequency. FCUR simulation is similar to FREQ, except that sea currents from CPL are also included in the surface boundary conditions in FCUR (updated every hour). In FREQ, the currents are zero, which is the common practice in atmosphere-only simulation. The FCUR simulation demonstrates the effect of currents relative to FREQ and the effect of coupling relative to CPL.

Table 1 summarises the simulations performed as part of this study. ens. stands for the number of ensemble members.

Dynamical contribution to changes in SST

To assess the dynamical contribution to changes in SST between simulations, we assumed quasi-steady-stated and small inertial forces to get the following equations for the surface winds

$$-f \cdot v = -\frac{1}{\rho}\frac{\partial p}{\partial x} + \frac{1}{\rho}\frac{\partial \tau_x}{\partial z} \tag{1}$$

$$f \cdot u = -\frac{1}{\rho}\frac{\partial p}{\partial y} + \frac{1}{\rho}\frac{\partial \tau_y}{\partial z} \tag{2}$$

where f is the Coriolis constant, u and v are the zonal and meridional winds, ρ is air density, p is the pressure, τ_x and τ_y are the zonal and meridional wind stress, and x, y, z are the standard Cartesian coordinates (eastward, northward and in the direction against gravity, respectively). By solving for wind speed, one can get the following

$$u^2 + v^2 = \frac{1}{f^2\rho^2}\left(\left[\left(\frac{\partial p}{\partial x}\right)^2 + \left(\frac{\partial p}{\partial y}\right)^2\right] + \frac{1}{H^2}\left[\tau_x^2 + \tau_y^2\right] + \frac{2}{H}\left[\frac{\partial p}{\partial x}\tau_x + \frac{\partial p}{\partial y}\tau_y\right]\right) \tag{3}$$

where H is the height of the surface layer. Here it is assumed that the wind stress at the surface is considerably larger than the other vertical levels, allowing us to neglect the upper-level stress. The first term in the square brackets represents the contribution of pressure, the second term is the contribution of wind stress, and the third term is an interaction term. Only the first two terms are plotted in the manuscript, assuming that if one of them is considerably smaller than the second (as shown in the text), their interaction is also small. Also, the

square root of the two terms was plotted, $\sqrt{(\partial p/\partial x)^2 + (\partial p/\partial y)^2}/(f\rho)$ and $\sqrt{\tau_x^2 + \tau_y^2}/(Hf\rho)$, to maintain an approximately linear relationship with the wind (up to a constant). Note that while the first and second terms in square brackets on the right-hand side are positive by definition, the third term can also be negative. Therefore, the sum of the first two terms can be, in principle, larger than the left side.

Cyclone track

Hourly best-track data for cyclones retrieved from[54]. This dataset has been built by combining 10 different Cyclone Detection and Tracking methods (CDTMs). These methods were applied to the hourly 0.25° ERA5 data spanning from 1979 to 2020. Here, we show the cyclone path as predicted by one of these algorithms (M05), but the others do not substantially differ from that track.

Data availability

ERA5 data is available on the Copernicus data store (https://cds.climate.copernicus.eu/cdsapp#!/dataset/reanalysis-era5-complete?tab=form). HYCOM data is available at the HYCOM website (https://ncss.hycom.org/thredds/ncss/grid/GLBv0.08/expt_93.0/dataset.html). IMERG data is available in the Copernicus data store (https://cds.climate.copernicus.eu/cdsapp#!/dataset/insitu-gridded-observations-global-and-regional?tab=form). IMS data is available from the IMS website (https://ims.gov.il/en/ObservationDataAPI). Some model output, configuration files, and plotting scripts are available in the Zenodo repository at: https://zenodo.org/records/10088418.

Code availability

The SKRIPS model code is available as a GitHub repository at: https://github.com/iurnus/scripps_kaust_model. Instructions on how to download the open-source model code and how to install it are available at: https://skrips.readthedocs.io/en/latest/.

Received: 9 June 2024; Accepted: 16 October 2024
Published online: 05 November 2024

References

1. Kushnir, Y. et al. Atmospheric gcm response to extratropical sst anomalies: Synthesis and evaluation. *J. Clim.* **15**, 2233–2256 (2002).
2. Hausmann, U. & Czaja, A. The observed signature of mesoscale eddies in sea surface temperature and the associated heat transport. *Deep Sea Res. Part I Oceanogr. Res. Pap.* **70**, 60–72 (2012).
3. Berthou, S. et al. Sensitivity of an intense rain event between atmosphere-only and atmosphere-ocean regional coupled models: 19 september 1996. *Q. J. R. Meteorol. Soc.* **141**, 258–271 (2015).
4. Pastor, F., Valiente, J. A. & Estrela, M. J. Sea surface temperature and torrential rains in the valencia region: modelling the role of recharge areas. *Nat. Hazards Earth Syst. Sci.* **15**, 1677–1693 (2015).
5. Goswami, B., Rao, S. A., Sengupta, D. & Chakravorty, S. Monsoons to mixing in the bay of bengal: Multiscale air-sea interactions and monsoon predictability. *Oceanography* **29**, 18–27 (2016).
6. Miglietta, M. M., Mazon, J., Motola, V. & Pasini, A. Effect of a positive sea surface temperature anomaly on a Mediterranean tornadic supercell. *Sci. Rep.* **7**, 12828. https://doi.org/10.1038/s41598-017-13170-0 (2017).
7. Hirons, L. C., Klingaman, N. P. & Woolnough, S. J. The impact of air-sea interactions on the representation of tropical precipitation extremes. *J. Adv. Model. Earth Syst.* **10**, 550–559 (2018).
8. Sun, R. et al. The role of air-sea interactions in atmospheric rivers: Case studies using the SKRIPS regional coupled model. *J. Geophys. Res. Atmos.* **126**, e2020JD032885. https://doi.org/10.1029/2020JD032885 (2021).
9. Jangir, B., Swain, D. & Ghose, S. K. Influence of eddies and tropical cyclone heat potential on intensity changes of tropical cyclones in the North Indian Ocean. *Adv. Sp. Res.* **68**, 773–786 (2021).
10. Jangir, B., Mishra, A. K. & Strobach, E. Effects of mesoscale eddies on the intensity of cyclones in the Mediterranean sea. *J. Geophys. Res. Atmos.* **128**, e2023JD038607. https://doi.org/10.1029/2023JD038607 (2023).
11. Ricchi, A. et al. Impact of the sst and topography on the development of a large-hail storm event, on the adriatic sea. *Atmos. Res.* **296**, 107078 (2023).
12. Ferrari, R. & Wunsch, C. Ocean circulation kinetic energy: Reservoirs, sources, and sinks. *Annu. Rev. Fluid Mech.* **41** (2009).
13. Klein, P. *et al.* Ocean-scale interactions from space. *Earth Sp. Sci.* (2019).
14. Liu, X. et al. Ocean fronts and eddies force atmospheric rivers and heavy precipitation in western North America. *Nat. Commun.* **12**, 1–10 (2021).
15. Foussard, A., Lapeyre, G. & Riwal, P. Storm tracks response to oceanic eddies in idealized atmospheric simulations. *J. Clim.* **32**, 445–463 (2019).
16. Strobach, E. *et al.* Local air-sea interactions at ocean mesoscale and submesoscale in a western boundary current. *Geophys. Res. Lett.* **49**, e2021GL097003 (2022).
17. Frenger, I., Gruber, N., Knutti, R. & Münnich, M. Imprint of southern ocean eddies on winds, clouds and rainfall. *Nat. Geosci.* **6**, 608 (2013).
18. Ma, X. et al. Western boundary currents regulated by interaction between ocean eddies and the atmosphere. *Nature* **535**, 533 (2016) (**Publisher: Nature Publishing Group.**).
19. Isern-Fontanet, J., Chapron, B., Lapeyre, G. & Klein, P. Potential use of microwave sea surface temperatures for the estimation of ocean currents. *Geophys. Res. Lett.* **33** (2006).
20. Meroni, A. N., Parodi, A. & Pasquero, C. Role of SST patterns on surface wind modulation of a heavy midlatitude precipitation event. *J. Geophys. Res. Atmos.* **123**, 9081–9096 (2018).
21. Toy, M. D. & Johnson, R. H. The influence of an SST front on a heavy rainfall event over coastal Taiwan during TiMREX. *J. Atmos. Sci.* **71**, 3223–3249 (2014).
22. Cassola, F., Ferrari, F., Mazzino, A. & Miglietta, M. M. The role of the sea on the flash floods events over Liguria (northwestern Italy). *Geophys. Res. Lett.* **43**, 3534–3542 (2016).
23. Foussard, A., Lapeyre, G. & Plougonven, R. Response of surface wind divergence to mesoscale sst anomalies under different wind conditions. *J. Atmos. Sci.* **76**, 2065–2082 (2019).
24. Hirata, H. & Nonaka, M. Impacts of strong warm ocean currents on development of extratropical cyclones through the warm and cold conveyor belts: A review. In *Tropical and Extratropical Air-Sea Interactions*. 267–293 (2021).

25. Fernández, V., Dietrich, D. E., Haney, R. L. & Tintoré, J. Mesoscale, seasonal and interannual variability in the mediterranean sea using a numerical ocean model. *Prog. Oceanogr.* **66**, 321–340 (2005) (mediterranean physical oceanography and biogeochemical cycles: Mediterranean general circulation and climate variability).
26. Isern-Fontanet, J., García-Ladona, E. & Font, J. Vortices of the mediterranean sea: An altimetric perspective. *J. Phys. Oceanogr.* **36**, 87–103 (2006).
27. Escudier, R. et al. Eddy properties in the western Mediterranean sea from satellite altimetry and a numerical simulation. *J. Geophys. Res. Oceans* **121**, 3990–4006 (2016).
28. Bonaduce, A. *et al.* Ocean mesoscale variability: A case study on the mediterranean sea from a re-analysis perspective. *Front. Earth Sci.* **9** (2021).
29. Amores, A., Jordà, G. & Monserrat, S. Ocean eddies in the mediterranean sea from satellite altimetry: Sensitivity to satellite track location. *Front. Mar. Sci.* **6** (2019).
30. Alpert, P., Neeman, B. U. & Shay-El, Y. Intermonthly variability of cyclone tracks in the Mediterranean. *J. Clim.* **3**, 1474–1478 (1990).
31. Flocas, H. A. et al. On cyclonic tracks over the eastern Mediterranean. *J. Clim.* **23**, 5243–5257 (2010).
32. Ziv, B., Harpaz, T., Saaroni, H. & Blender, R. A new methodology for identifying daughter cyclogenesis: Application for the mediterranean basin. *Int. J. Climatol.* **35**, 3847–3861 (2015).
33. Flaounas, E. et al. Mediterranean cyclones: current knowledge and open questions on dynamics, prediction, climatology and impacts. *Weather Clim. Dyn.* **3**, 173–208 (2022).
34. Michaelides, S. *et al.* Reviews and perspectives of high impact atmospheric processes in the Mediterranean. *Atmos. Res.* **208**, 4–44 (2018) (high impact atmospheric processes in the Mediterranean).
35. Meroni, A. N., Giurato, M., Ragone, F. & Pasquero, C. Observational evidence of the preferential occurrence of wind convergence over sea surface temperature fronts in the Mediterranean. *Q. J. R. Meteorol. Soc.* **146**, 1443–1458 (2020).
36. Desbiolles, F., Alberti, M., Hamouda, M. E., Meroni, A. N. & Pasquero, C. Links between sea surface temperature structures, clouds and rainfall: Study case of the Mediterranean Sea. *Geophys. Res. Lett.* **48** (2021).
37. Mishra, A. K., Jangir, B. & Strobach, E. Does increasing climate model horizontal resolution be beneficial for the Mediterranean region?: Multimodel evaluation framework for high-resolution model intercomparison project. *J. Geophys. Res. Atmos.* **128**, e2022JD037812. https://doi.org/10.1029/2022JD037812 (2023).
38. O'Reilly, C. H., Minobe, S. & Kuwano-Yoshida, A. The influence of the gulf stream on wintertime European blocking. *Clim. Dyn.* **47**, 1545–1567 (2016).
39. Drori, R., Ziv, B., Saaroni, H., Etkin, A. & Sheffer, E. Recent changes in the rain regime over the Mediterranean climate region of Israel. *Clim. Change* **167**, 15 (2021).
40. Small, R. J. et al. Air-sea interaction over ocean fronts and eddies. *Dyn. Atmos. Oceans* **45**, 274–319 (2008).
41. Seo, H. et al. Ocean mesoscale and frontal-scale ocean-atmosphere interactions and influence on large-scale climate: A review. *J. Clim.* **36**, 1981–2013 (2023).
42. Wallace, J. M., Mitchell, T. P. & Deser, C. The influence of sea-surface temperature on surface wind in the eastern equatorial pacific: Seasonal and interannual variability. *J. Clim.* **2**, 1492–1499 (1989).
43. Lindzen, R. S. & Nigam, S. On the role of sea surface temperature gradients in forcing low-level winds and convergence in the tropics. *J. Atmos. Sci.* **44**, 2418–2436 (1987).
44. Meroni, A. N., Desbiolles, F. & Pasquero, C. Introducing new metrics for the atmospheric pressure adjustment to thermal structures at the ocean surface. *J. Geophys. Res. Atmos.* **127**, e2021JD035968 (2022).
45. Ma, J., Xu, H., Dong, C., Lin, P. & Liu, Y. Atmospheric responses to oceanic eddies in the Kuroshio extension region. *J. Geophys. Res. Atmos.* **120**, 6313–6330 (2015).
46. Ma, X. et al. Importance of resolving kuroshio front and eddy influence in simulating the north pacific storm track. *J. Clim.* **30**, 1861–1880 (2017).
47. Liu, X., Chang, P., Kurian, J., Saravanan, R. & Lin, X. Satellite-observed precipitation response to ocean mesoscale eddies. *J. Clim.* **31**, 6879–6895 (2018).
48. Renault, L. et al. Modulation of wind work by oceanic current interaction with the atmosphere. *J. Phys. Oceanogr.* **46**, 1685–1704 (2016).
49. Bai, Y. et al. Sub-mesoscale wind-front interactions: The combined impact of thermal and current feedback. *Geophys. Res. Lett.* **50**, e2023GL104807 (2023).
50. Su, Z., Wang, J., Klein, P., Thompson, A. F. & Menemenlis, D. Ocean submesoscales as a key component of the global heat budget. *Nat. Commun.* **9**, 775 (2018).
51. Gaspar, P., Grégoris, Y. & Lefevre, J.-M. A simple eddy kinetic energy model for simulations of the oceanic vertical mixing: Tests at station papa and long-term upper ocean study site. *J. Geophys. Res. Oceans* **95**, 16179–16193 (1990).
52. Hersbach, H. et al. The era5 global reanalysis. *Q. J. R. Meteorol. Soc.* **146**, 1999–2049 (2020).
53. Hycom + ncoda global $1/12^{\circ}$ reanalysis. https://www.hycom.org/dataserver/gofs-3pt0/reanalysis. Accessed 20 Mar 2023 (2023).
54. Flaounas, E. et al. A composite approach to produce reference datasets for extratropical cyclone tracks: application to mediterranean cyclones. *Weather Clim. Dyn.* **4**, 639–661 (2023).

Acknowledgements

This research was supported by the Israel Science Foundation (grants no. 2228/21 and 2253/20). PK acknowledges support from the SWOT/JPL Science Team.

Author contributions

ES and PK have designed the model experiments. ES ran the model, analyzed the data, and generated the figures. ANM calculated and plotted the air-sea interaction indices. All authors have participated in writing and reviewing the manuscript.

Declarations

Competing Interests

The authors declare no competing interests.

Additional information

Supplementary Information The online version contains supplementary material available at https://doi.org/10.1038/s41598-024-76767-2.

Correspondence and requests for materials should be addressed to E.S.